CHEMISTRY OF MATERIALS

ARTICLE

pubs.acs.org/cm

Structural Disorder in Doped Zirconias, Part I: The $Zr_{0.8}Sc_{0.2-x}Y_xO_{1.9}$ $(0.0 \leq x \leq 0.2)$ System

Stefan T. Norberg,*[†,‡] Stephen Hull,[†] Istaq Ahmed,[‡] Sten G. Eriksson,[‡] Dario Marrocchelli,[§,¶] Paul A. Madden,[∥] Peng Li,[⊥,#] and John T. S. Irvine[⊥]

[†]The ISIS Facility, Rutherford Appleton Laboratory, Chilton, Didcot OX11 0QX, United Kingdom
[‡]Department of Chemical and Biological Engineering, Chalmers University of Technology, SE-412 96 Gothenburg, Sweden
[§]School of Chemistry, University of Edinburgh, Edinburgh EH9 3JJ, United Kingdom
[∥]Department of Materials, University of Oxford, Park Road, Oxford OX1 3PH, United Kingdom
[⊥]School of Chemistry, University of St Andrews, St Andrews KY16 9ST, United Kingdom
[#]State Key Laboratory of Solidification Processing, Northwestern Polytechnical University, Xi'an 710072, P.R. China

ABSTRACT: The influence of local ordering of the anion vacancies and cation−anion vacancy interactions on the ionic conductivity of the anion-deficient fluorite $Zr_{0.8}Sc_{0.2-x}Y_xO_{1.9}$ $(0.0 \leq x \leq 0.2)$ system have been investigated using impedance spectroscopy, molecular dynamics (MD) simulations, and reverse Monte Carlo (RMC) analysis of neutron powder diffraction data. At 1000 K, the ionic conductivity decreases by a factor of ∼2 as x increases from 0.0 to 0.2, while the oxygen anion partial radial distribution function, $g_{OO}(r)$, remains similar across the entire solid solution, even though the cation−oxygen interactions change with increasing Y_2O_3 content. These experimental data are used to validate the MD simulations, which probe the details of the vacancy−vacancy interactions within the $x = 0.0$ and $x = 0.2$ end members. Both possess similar vacancy−vacancy ordering that favors the formation of pairs along ⟨111⟩ directions. Significantly, an increased proportion of the oxygen vacancies are associated with the Zr^{4+} cations in $Zr_{0.8}Y_{0.2}O_{1.9}$, while in $Zr_{0.8}Sc_{0.2}O_{1.9}$ they show no significant preference for being nearest neighbor to a Sc^{3+} or a Zr^{4+} cation. Thus, it is concluded that the lower ionic conductivity at $x = 0.2$ is predominantly a consequence of the larger size of the Y^{3+} cation, which induces strain in the lattice and hinders diffusion of the O^{2-}, rather than changes in the local ordering of the anion vacancies.

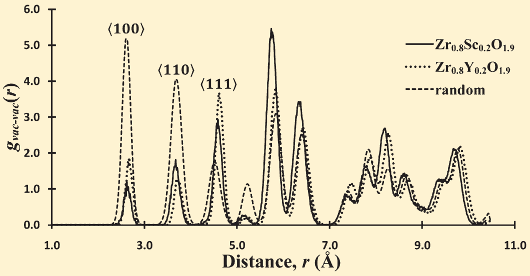

KEYWORDS: RMC and MD modeling, neutron diffraction, oxygen vacancy ordering, doped zirconia (ZrO_2), SOFC electrolytes

1. INTRODUCTION

Fuel cell technology currently attracts significant attention since these devices show considerable potential for efficient power generation in stationary, portable, and transport applications.[1] Their main advantage is the combination of low emissions of pollutants, coupled with a high efficiency for the conversion of chemical energy into electrical energy. For example, the use of solid oxide fuel cell (SOFCs) systems running on conventional fossil fuels producing no emissions of sulphurous, nitric, and hydrocarbon pollutants, plus a greatly reduced CO_2 emission, gives significant environmental advantages over conventional power generation systems. The core component within an SOFC is the impermeable solid electrolyte, which consists of a polycrystalline oxide ceramic operating at temperatures between 1000 and 1300 K.[1] The high SOFC operating temperature means, for example, that conventional hydrocarbon fuels can be used without the need for expensive catalysts. However, it also places severe demands on the materials used for SOFC components such as the interconnect, cathode, anode, and solid electrolyte, since the use of complex (and expensive) ceramics and alloys becomes necessary. Operating at lower temperatures would allow for low chromium content steels to be utilized and so reduces risk of degradation from chrome poisoning.[2] As a consequence, there is significant motivation to reduce the SOFC operating temperature to an intermediate range of around 800−1000 K, and a substantial research effort is currently focused on developing improved ceramic electrolytes to meet such applications.

The current SOFC electrolyte of choice is yttria stabilized zirconia (YSZ, $Zr_{1-x}Y_xO_{2-x/2}$) which, for $x > 0.16$, adopts the cubic fluorite phase[3] (see Figure 1), in which a fraction $(x/4)$ of the anion sites are vacant to compensate for the lower charge of the dopant Y^{3+} cation compared to the host Zr^{4+}. The oxygen anion conductivity, σ, increases with increasing x, until a maximum value $(\sigma \sim 10^{-2}\ \Omega^{-1}\ cm^{-1}$ at 1000 K) is reached at an yttria concentration close to the lower stability limit of the cubic fluorite phase.[4] The ionic conductivity of zirconia doped with aliovalent cations is now widely accepted to occur via the migration of isolated anion vacancies. However, a simple picture of uncorrelated diffusion of anion vacancies through the crystal lattice cannot account for the variation of σ of systems such as $Zr_{1-x}Y_xO_{2-x/2}$ with dopant concentration x.

Received: September 29, 2010
Revised: January 18, 2011
Published: February 23, 2011

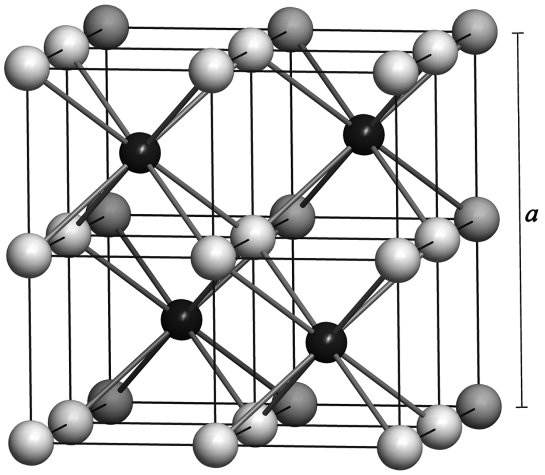

Figure 1. Cubic fluorite structure ($Fm\bar{3}m$) with cations at the 4(a) sites at 0, 0, 0, etc., and the oxygen atoms at the 8(c) sites at 1/4, 1/4, 1/4, etc.

In particular, the decrease in the ionic conductivity above $x \sim 0.16$ has provided a challenge to both experimental and theoretical approaches. X-ray[5−10] and neutron[11−18] diffraction studies show that significant fractions of the ions are displaced off their regular lattice sites. Pronounced diffuse scattering has been interpreted by Goff et al.[18] in terms of short-range correlations between anion vacancies, which preferentially form pairs in ⟨111⟩ directions and aggregate to hamper ionic diffusion at high values of x. However, these studies provide little insight into the role of interactions between the anion vacancies and the host/dopant cations, largely due to the low contrast in the X-ray and neutron scattering powers of Zr^{4+} and Y^{3+}. Early theoretical studies by Hohnke[19] showed that a simple model of a bound dopant cation−anion vacancy pair could reproduce the peak in σ, while Catlow[20] demonstrated that the aggregation of dopant cations creates deep traps which immobilize vacancies. More recent computational work by Bogicevic et al.[21] has shown that the larger strain component associated with the dopant cations results in a preferential binding of vacancies to the smaller (Zr^{4+}) cations.

Alternatives to YSZ which show higher σ at lower temperature include gadolinium-doped ceria,[22,23] lanthanum based gallates,[24−27] and a number of bismuth based electrolytes.[28] However, it is also possible to increase the anion conductivity in YSZ by substituting Y^{3+} by Sc^{3+},[29] and scandium stabilized zirconia (SSZ) electrolytes show good potential for use in SOFCs operating at temperatures below ~1000 K. From the crystal structure point-of-view, SSZ is rather more complex than its YSZ counterpart, and the stability field of the highly conducting cubic fluorite structured phase is more limited in composition and temperature. As a result of the highly refractory nature of the scandia zirconia system it can be quite difficult to achieve thermodynamic equilibrium, and hence there are some apparent disagreements about phase equilibria in the literature; however, the system is broadly understood. The room temperature monoclinic ($P2_1/c$) phase is stable with scandia content below $x \sim 0.04$, with increased doping favoring a tetragonal ($P4_2/nmc$) phase which is pure from $\sim 0.10 \le x \le 0.15$. Slightly higher levels of Sc^{3+} doping result in a mixed phase system containing both a poorly conducting rhombohedral ($R\bar{3}$) phase (the so-called β-phase) and the highly conducting cubic ($Fm\bar{3}m$) phase with a fluorite structure.[30,31] Even higher scandia contents, above $x \sim 0.19$, results in phases such as $Zr_{50}Sc_{12}O_{118}$ ($x = 0.194$),[32] $Zr_7Sc_2O_{17}$ ($x = 0.222$),[30] $Zr_5Sc_2O_{13}$ ($x = 0.286$),[33] and $Zr_3Sc_4O_{12}$ ($x = 0.571$)[33] in which the anion vacancies are predominantly ordered over long distances. Politova and Irvine[34] showed that the highly conducting cubic modification of SSZ can be stabilized at room temperature as a single phase by the addition of Y_2O_3, with only $x \sim 0.02$ in $Zr_{0.8}Sc_{0.2-x}Y_xO_{1.9}$ required to suppress the β-phase. However, the ionic conductivity of the solid solution decreases with Y^{3+} content x. This study uses a combination of impedance spectroscopy, neutron powder diffraction, and molecular dynamics (MD) simulations to probe the anion vacancy ordering in $Zr_{0.8}Sc_{0.2-x}Y_xO_{1.9}$ and assess the roles of vacancy−vacancy and cation−vacancy interactions in determining the ionic conductivity of the system as a function of x. A subsequent MD study[35] will extend this methodology to probe the effects of vacancy−vacancy clustering and size mismatch between host and dopant cations on the ionic conductivity in stabilized zirconias, $Zr_{1-x}M_xO_{2-x/2}$ (M = Sc or Y).

2. EXPERIMENTAL AND COMPUTATIONAL METHODS

2.1. Sample Preparation. $Zr_{0.8}Sc_{0.2-x}Y_xO_{1.9}$ powder samples with x = 0.0, 0.04, 0.08, 0.12, 0.16, and 0.2 of typical volumes of 2.5 cm^3 were prepared by mixing stoichiometric amounts of the previously dried binary oxides ZrO_2, Sc_2O_3, and Y_2O_3 supplied by the Aldrich Chemical Co. and of stated purities 99.99%, 99.999%, and 99.99%, respectively. High purity HfO_2-free zirconia powder was used to avoid the significant neutron absorption caused by hafnium contamination. The starting powders were mixed and thoroughly ground by a planetary ball mill using zirconia balls and a zirconia jar for 8 h and thereafter pressed into pellets that were heated at 1873 K for 16 h. The sintered pellets were subsequently crushed, ball milled again, pressed, and sintered at 1873 K for another 16 h to obtain homogeneous samples. Samples used for neutron diffraction were subsequently crushed and ground into a fine powder. After the neutron diffraction experiments the samples were resintered into pellets at 1773 K for 10 h and used for impedance spectroscopy studies.

2.2. Impedance Spectroscopy. The total (bulk plus grain boundary) ionic conductivity of the $Zr_{0.8}Sc_{0.2-x}Y_xO_{1.9}$ samples with $0.0 \le x \le 0.2$ was measured on sample pellets of approximately 10 mm diameter and 1 mm height using platinum electrodes and a voltage of 50 mV. Platinum paste was used to ensure good contact between the electrodes and the sample. The samples were then heated to 1173 K in air, and the complex impedance spectroscopy was performed during cooling at 50 K intervals, using a Solartron SI 1260 frequency response analyzer over a frequency range from 1 Hz to 13 MHz. The total conductivity was determined by least-squares equivalent circuit fitting to the frequency dependent impedance data using the program ZVIEW.

2.3. Neutron Powder Diffraction. Neutron diffraction experiments were performed at the Polaris diffractometer of the ISIS facility, Rutherford Appleton Laboratory, U.K.,[36] using the backscattering detector bank (covering scattering angles of $130° < 2\theta < 160°$), the ~90° detector bank ($85° < 2\theta < 95°$), and the low angle detector bank ($28° < 2\theta < 42°$). These cover approximate ranges of scattering vector Q (where $Q = 2\pi/d$ and d is the interplanar spacing) of 2−30 $Å^{-1}$, 1.5−20 $Å^{-1}$ and 0.8−12 $Å^{-1}$, respectively. Each powder sample was encapsulated in a cylindrical 6 mm diameter thin-walled (40 μm) vanadium can and measured for approximately 12 h to obtain counting statistics of sufficient statistical quality to allow analysis of the total (Bragg plus diffuse scattering components) scattering. Preliminary Rietveld analysis of the averaged structures using only the Bragg scattering was performed using the GSAS software.[37]

2.4. Neutron Total Scattering. After correction for the effects of background scattering and beam attenuation, the diffraction data from each detector bank was merged to a single spectrum covering a wide Q range using the program *Gudrun*.[38] This process also puts the scattered intensity onto an absolute scale of scattering cross-section. The resultant normalized total scattering structure factor, $S(Q)$, was used to generate the corresponding total radial distribution function, $G(r)$, via a Fourier transform

$$G(r) = \frac{1}{(2\pi)^3\rho_0}\int_0^\infty 4\pi Q^2 S(Q)\frac{\sin Qr}{Qr}\,dQ \qquad (1)$$

where ρ_0 is the average atom number density in atoms Å^{-3} (for details, see Keen[39]).

The $G(r)$ can also be expressed in terms of the individual partial radial distribution functions, $g_{ij}(r)$, weighted by the concentrations of the two species, c_i and c_j, and their coherent bound neutron scattering lengths, $\bar{b}_i$ and $\bar{b}_j$, so that

$$G(r) = \sum_{i,j=1}^{n} c_i c_j \bar{b}_i \bar{b}_j g_{ij}(r) \Big/ \sum_{i=1}^{n} (c_i \bar{b}_i)^2 \qquad (2)$$

where n is the number of ionic species. The partial radial distribution function is in turn given by

$$g_{ij}(r) = \frac{1}{4\pi r^2 \Delta r}\frac{n_{ij}(r)}{\rho_j} \qquad (3)$$

with $n_{ij}(r)$ equal to the number of atoms of type j located at a distance between r and $r + \Delta r$ from an atom of type i and ρ_j the number density of atoms of type j, given by $\rho_j = c_j\rho_0$. These individual partial distribution functions, $g_{ij}(r)$, can be obtained from RMC modeling, which simultaneously probes both the long-range and short-range structural properties.

2.5. RMC Modeling Details. RMC analysis[40] of the neutron total scattering data (Bragg peaks plus diffuse scattering components) was performed using the *RMCProfile* software.[41] Each RMC model, one for each sample stoichiometry, used a configuration box of 10 × 10 × 10 unit cells (i.e., contains a total of 4000 $Zr^{4+}/Sc^{3+}/Y^{3+}$ cations in their stoichiometric ratio and 7600 O^{2-} anions, with all ions randomly distributed over their regular crystallographic sites). A bond valence sum (BVS) soft constraint[42] was used to ensure that individual cation−anion coordination environments remain chemically reasonable, with parameters taken from Brese and O'Keeffe.[43] The RMC modeling used both reciprocal space data, $S(Q)$, and real space data, $G(r)$. The former emphasizes the long-range ordering while the $G(r)$ focuses on the short-range interactions. Additionally, the $S(Q)$ is broadened by convolution with a box function to reflect the finite size of the configuration box (for details, see[41]). The broadened $S_{box}(Q)$ is used in the RMC method, and the comparison between the calculated functions and the experimental data is assessed using an agreement factor given by

$$\chi_{RMC}{}^2 = \sum_j \chi_j{}^2 \qquad (4)$$

where $\chi_j{}^2$ is the individual agreement factor for data type j.

2.6. Interionic Potentials. The interaction potential used in this study is the dipole polarizable ion model (DIPPIM), and since the procedure for parameter optimization has been thoroughly described elsewhere,[44,45] only a brief overview will be provided here. The model allows the ionic species to carry their formal valence charges (Zr^{4+}, Sc^{3+}, Y^{3+}, and O^{2-}), and polarization effects, resulting from the induction of dipoles on the ions, are included. The parameters of the interaction potential for the $Zr_{0.8}Sc_{0.2-x}Y_xO_{1.9}$ system were obtained by a force- and dipole-matching procedure aimed at reproducing a large set of first-principle (DFT) reference data on the condensed phase.[44] More than 2000 data points, comprising the three Cartesian force components of each ion and the three components for the dipole, were used in this procedure. Such potentials have been shown to provide an accurate and transferable representation of the interactions in a number of oxides (see, for example, studies related to the $Zr_2Y_2O_7$−Y_3NbO_7[45,46] system and GeO_2[47,48]). One potential deficiency is that the parent DFT calculations do not accurately represent the dispersion interactions between the ions, requiring an empirical adjustment to obtain the correct density. The parameters used in this study are reported in Table 1.

Table 1. Parameters for the DIPPIM Potentials with Values Given in a.u.[a]

	O−O	Y−O	Zr−O	Sc−O
A^{ij}	0.00	83.11	65.50	59.19
a^{ij}	5.00	1.294	1.206	1.275
B^{ij}	50000	50000	50000	50000
b^{ij}	1.00	1.25	1.50	1.50
α	14.33	1.90	2.33	1.20
C_6^{ij}	66	15	7	7
C_8^{ij}	1200	300	150	150
b_{disp}^{ij}	1.2	1.9	1.9	1.9
b_D^{O-O}	1.736	b_D^{O-Zr}	1.817	
c_D^{O-O}	0.874	c_D^{O-Zr}	1.720	
b_D^{O-Y}	1.700	b_D^{Y-Y}	1.926	
c_D^{O-Y}	1.559	c_D^{Y-Y}	−1.766	
b_D^{O-Sc}	1.832	b_D^{Y-O}	1.700	
c_D^{O-Sc}	1.666	c_D^{Y-O}	−2.486	
b_D^{Sc-Sc}	1.926	b_D^{Sc-O}	1.832	
c_D^{Sc-Sc}	−1.766	c_D^{Sc-O}	−2.797	
b_D^{Zr-Zr}	1.135	b_D^{Zr-O}	1.817	
c_D^{Zr-Zr}	0.373	c_D^{Zr-O}	−2.499	

[a] Only those short-range parameters not equal to zero are reported. See Norberg et al.[45] for further information concerning the DIPPIM potential parameters.

2.7. MD Simulation Details. All the MD simulations on the $Zr_{0.8}Sc_{0.2-x}Y_xO_{1.9}$ system were performed, unless stated otherwise, using a cubic configuration box of 4 × 4 × 4 unit cells, that is, 256 cations and 486 oxygen anions. The ions were randomly distributed over their average positions, as for the RMC modeling (see Section 2.5). The time step used was 1 fs. Coulombic and dispersion interactions were summed using Ewald summations, while the short-range part of the potential was truncated to half the length of the simulations box (usually ∼10 Å). High temperature runs, used to evaluate the ionic conductivity of these materials, were performed at constant volume and temperature (NVT ensemble). Room temperature runs, used to obtain structural information such as the radial distribution functions, were performed at constant pressure and temperature (NPT ensemble). The latter were obtained by first equilibrating the system at 1800−2000 K for 50 ps and then slowly cooling to 300 K, with a cooling rate of 34 K/ps.

3. RESULTS AND DISCUSSION

3.1. Ionic Conductivity. Figure 2 shows the temperature dependence of the total conductivity data for the $Zr_{0.8}Sc_{0.2-x}Y_xO_{1.9}$ samples with $0.0 \leq x \leq 0.2$. These data are in excellent agreement with those reported previously for the case of $Zr_{0.8}Y_{0.2}O_{1.9}$ and $Zr_{0.8}Sc_{0.2}O_{1.9}$[34] and indicate the presence of a phase transition to the cubic fluorite structured phase in the latter material at ∼900 K (see below). At temperatures of ∼1000 K there is a clear trend of decreasing σ with increasing Y^{3+} content x, which forms the focus of this study.

3.2. Rietveld Refinement. Long-range average structure models were determined for the $Zr_{0.8}Sc_{0.2-x}Y_xO_{1.9}$ samples with $x > 0$ using conventional Rietveld refinement.[49] In the case of $Zr_{0.8}Sc_{0.2}O_{1.9}$, the diffraction data indicated the presence of rhombohedral, cubic, and at least one other unidentified phases and it was not possible to perform a successful refinement for the

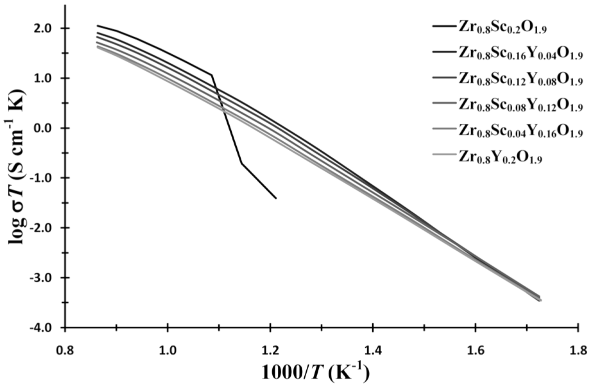

Figure 2. Total conductivity plots for the $Zr_{0.8}Sc_{0.2-x}Y_xO_{1.9}$ compounds. Increasing amount of Y^{3+} decreases the conductivity at high temperatures.

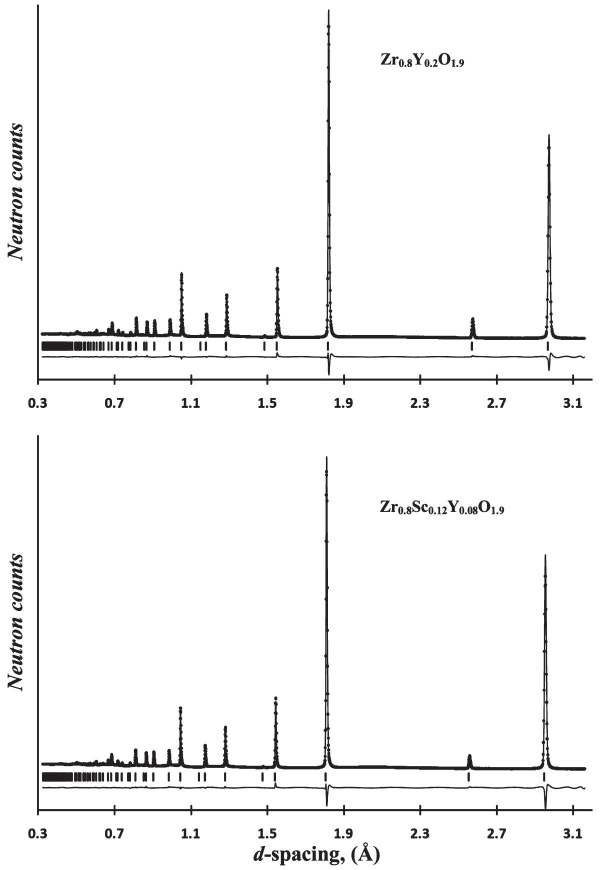

Figure 3. Rietveld fit to the neutron powder diffraction data collected from (top) $Zr_{0.8}Y_{0.2}O_{1.9}$ and (bottom) $Zr_{0.8}Sc_{0.12}Y_{0.08}O_{1.9}$, with the dots showing the experimental data and the solid line showing the fitted profile. The short vertical lines indicate allowed Bragg reflections, and the difference between observed and calculated is plotted below.

Table 2. Experimental Values of the Cubic Lattice Parameter, a_{exp}, at Ambient Temperature and the Corresponding Values Obtained from the MD Simulations at 300 K, a_{MD}[a]

	a_{exp} (Å)	a_{MD} (Å)
$Zr_{0.8}Sc_{0.2}O_{1.9}$	5.08379(2)	5.135
$Zr_{0.8}Sc_{0.16}Y_{0.04}O_{1.9}$	5.10069(2)	5.146
$Zr_{0.8}Sc_{0.12}Y_{0.08}O_{1.9}$	5.11188(2)	5.166
$Zr_{0.8}Sc_{0.08}Y_{0.12}O_{1.9}$	5.12371(2)	5.173
$Zr_{0.8}Sc_{0.04}Y_{0.16}O_{1.9}$	5.13686(2)	5.182
$Zr_{0.8}Y_{0.2}O_{1.9}$	5.14878(2)	5.195

[a] Fluorite bond distances: $M-O = a\sqrt{(3/4)}$; $O-O = a/2$; $M-M = a/\sqrt{2}$.

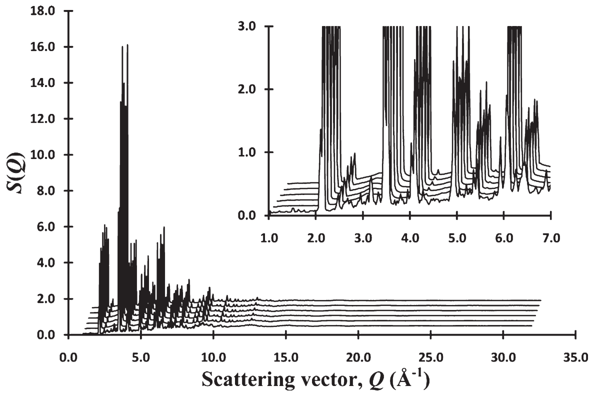

Figure 4. Experimental $S(Q)$ values for the $Zr_{0.8}Sc_{0.2-x}Y_xO_{1.9}$ compounds, from $x = 0.0$ (bottom) to $x = 0.2$ (top).

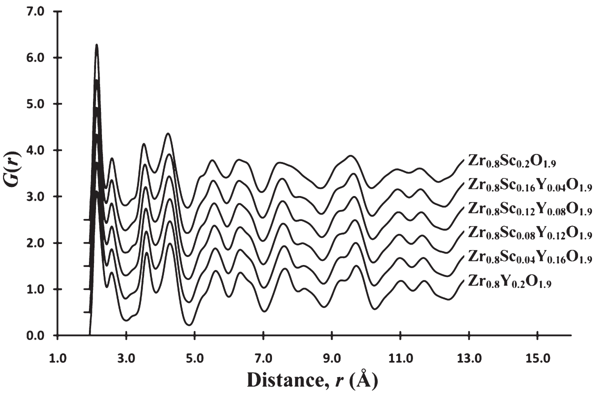

Figure 5. Experimental total radial distribution functions, $G(r)$, as calculated by Fourier transform of the normalized total scattering data, $S(Q)$.

small fraction of unknown phase at room temperature. The refined parameters consisted of a scale factor, an extinction factor, the cubic lattice parameter a, isotropic thermal vibration parameters for each crystallographic site, u_{cation}, and u_O, plus 36 coefficients of a shifted Chebyshev polynomial describing the undulating background scattering and two coefficients describing Gaussian and Lorentzian contributions to the Bragg peak shapes. Excellent fits were obtained using cation ratios based on the sample preparation (see the example of $Zr_{0.8}Y_{0.2}O_{1.9}$, and $Zr_{0.8}Sc_{0.12}Y_{0.08}O_{1.9}$ in Figure 3), and the refined values of the lattice parameters listed in Table 2 show the marked increase in a with x which reflects the larger ionic radius of Y^{3+} compared to Sc^{3+}.[50]

3.3. Total Scattering Analysis. Figure 4 shows the normalized total scattering function $S(Q)$ for all the samples, from $Zr_{0.8}Sc_{0.2}O_{1.9}$ (bottom) to $Zr_{0.8}Y_{0.2}O_{1.9}$ (top), and Figure 5 illustrates the corresponding total radial distribution function $G(r)$ obtained by Fourier transform of $S(Q)$ (eq 1). Note that the changes in the $G(r)$ patterns show a clear trend across all measured samples, even though the $S(Q)$ for the mixed phase $Zr_{0.8}Sc_{0.2}O_{1.9}$ sample differs significantly from the other (cubic structured) samples. This suggests that the

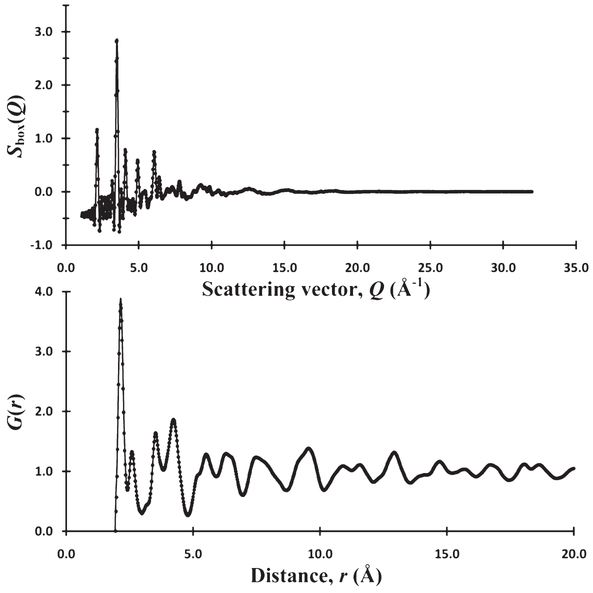

Figure 6. $S_{box}(Q)$ and the $G(r)$ fits obtained by RMC modeling for $Zr_{0.8}Sc_{0.2}O_{1.9}$. The dots show the experimental data, and the solid line shows the calculated profile.

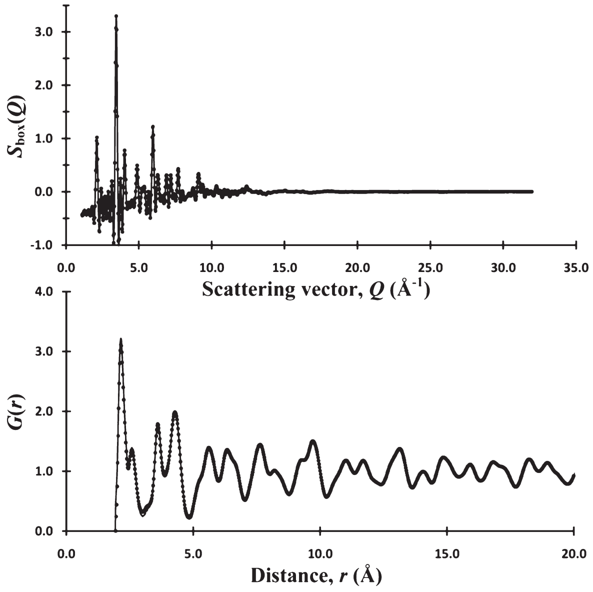

Figure 7. $S_{box}(Q)$ and the $G(r)$ fits obtained by RMC modeling for $Zr_{0.8}Y_{0.2}O_{1.9}$. The dots show the experimental data, and a solid line shows the calculated profile.

Table 3. Comparison of the χ^2 Values for the Fits to $S(Q)$ and $G(r)$ for All Samples

	$S(Q)$	$G(r)$
$Zr_{0.8}Sc_{0.2}O_{1.9}$	16.2	11.6
$Zr_{0.8}Sc_{0.16}Y_{0.04}O_{1.9}$	44.8	16.3
$Zr_{0.8}Sc_{0.12}Y_{0.08}O_{1.9}$	48.7	14.9
$Zr_{0.8}Sc_{0.08}Y_{0.12}O_{1.9}$	59.7	13.2
$Zr_{0.8}Sc_{0.04}Y_{0.16}O_{1.9}$	44.2	14.3
$Zr_{0.8}Y_{0.2}O_{1.9}$	50.0	13.5

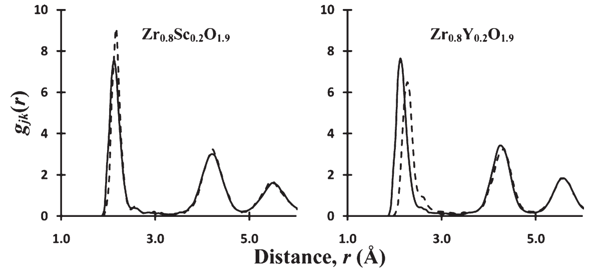

Figure 8. Partial radial distribution functions, $g_{jk}(r)$, as determined by RMC modeling. $Zr_{0.8}Sc_{0.2}O_{1.9}$ (left): $g_{ZrO}(r)$ and $g_{ScO}(r)$, solid and dashed line, respectively; $Zr_{0.8}Y_{0.2}O_{1.9}$ (right): $g_{ZrO}(r)$ and $g_{YO}(r)$, solid and dashed line, respectively.

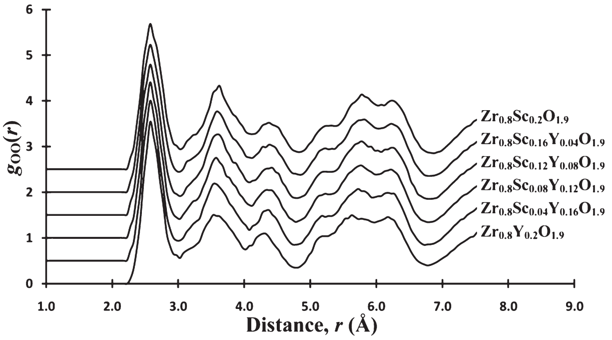

Figure 9. Partial radial distribution function, $g_{OO}(r)$, for the $Zr_{0.8}Sc_{0.2-x}Y_xO_{1.9}$ samples, as determined by RMC modeling.

local structure is relatively unchanged with x, irrespective of the long-range (crystallographic) arrangement. The most noticeable change is the continuous narrowing of the peaks at 2.14 and 2.58 Å as x decreases, which indicates a successively more uniform cation oxygen bond length distribution.

Turning to the RMC analysis, the quality of the final fit to both the $S_{box}(Q)$ and the $G(r)$ for the $x = 0.2$ and $x = 0.0$ end members of the series $Zr_{0.8}Sc_{0.2-x}Y_xO_{1.9}$ is shown in Figures 6 and 7, respectively (see Table 3 for a comparison of the χ^2 values obtained for the fits to $S(Q)$ and $G(r)$ for all $Zr_{0.8}Sc_{0.2-x}Y_xO_{1.9}$ members). Figure 8 shows the cation−anion partial radial distribution functions for these two compounds, extracted from the final RMC configurations. In the case of $Zr_{0.8}Sc_{0.2}O_{1.9}$, the first peak in the $g_{ZrO}(r)$ and $g_{ScO}(r)$ indicates average bond distances of 2.188 Å and 2.209 Å, for $Zr^{4+}-O^{2-}$ and $Sc^{3+}-O^{2-}$, respectively. However, for $Zr_{0.8}Y_{0.2}O_{1.9}$ the first peak in the $g_{ZrO}(r)$ and $g_{YO}(r)$ gives average bond distances of 2.195 Å and 2.330 Å, for $Zr^{4+}-O^{2-}$ and $Y^{3+}-O^{2-}$, respectively. Thus, there is a significant mismatch between the anion environment around the dopant and host cations in the latter sample, which is consistent with the ionic radii for these cations, that is, Zr^{4+} 0.84 Å, Sc^{3+} 0.87 Å, and Y^{3+} 1.02 Å,[50] and is reflected in the average cation−oxygen bond distances of 2.20 Å ($Zr_{0.8}Sc_{0.2}O_{1.9}$) and 2.23 Å ($Zr_{0.8}Y_{0.2}O_{1.9}$) obtained from the Rietveld refinements.

For the anion−anion correlations, Figure 9 shows the $g_{OO}(r)$ partial radial distribution functions extracted from the RMC analysis for the $Zr_{0.8}Sc_{0.2-x}Y_xO_{1.9}$ series. There are no significant changes in the $g_{OO}(r)$ from one end member to the other, suggesting that any preferential short-range ordering of the vacancies is very similar in all the samples (see next section). The position of the first peak in $g_{OO}(r)$ is at roughly 2.58 Å for all the $Zr_{0.8}Sc_{0.2-x}Y_xO_{1.9}$ samples, which agrees well with the value of 2.55 Å to 2.57 Å obtained from the Rietveld analysis. Thus, on

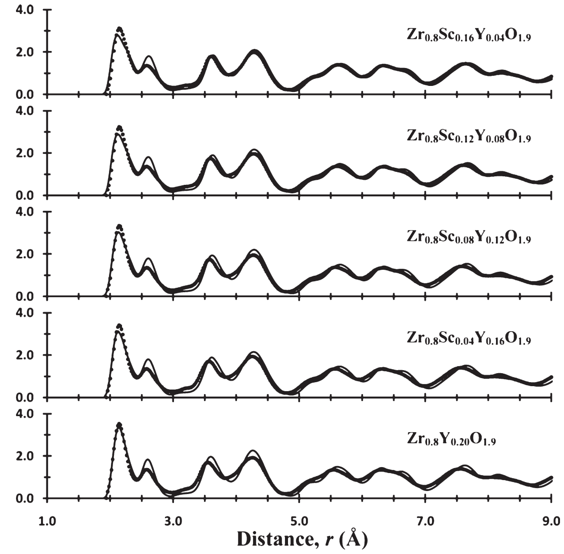

Figure 10. Comparison between the experimental (dotted line) and simulated (solid line) total $G(r)$ values for the $Zr_{0.8}Sc_{0.2-x}Y_xO_{1.9}$ system at 300 K.

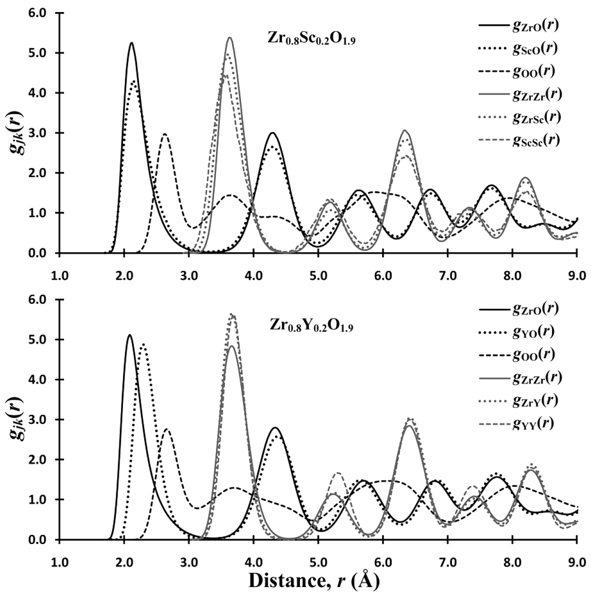

Figure 11. Partial radial distribution functions, $g_{jk}(r)$, obtained by MD simulations at 1200 K for (*a*) $Zr_{0.8}Sc_{0.2}O_{1.9}$ and (*b*) $Zr_{0.8}Y_{0.2}O_{1.9}$.

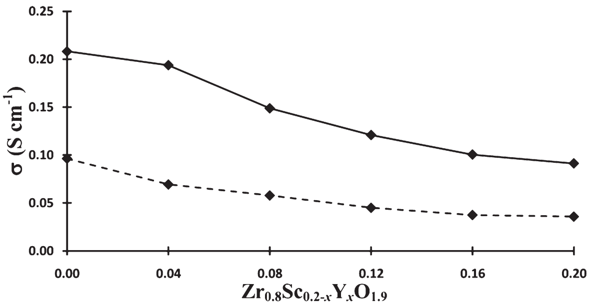

Figure 12. Comparison of experimental (1158 K, dashed line) and calculated (1200 K, solid line) oxygen anion conductivity for $Zr_{0.8}Sc_{0.2-x}Y_xO_{1.9}$.

a local scale, the ionic arrangement is very similar to the long-range average (cubic fluorite) structure in these materials. This contrasts with the case of the closely related $Y_2Zr_2O_7$–Y_3NbO_7 series,[45] in which the addition of Nb^{5+} causes a significant local distortion of its surrounding anion shell toward an octahedral coordination, with a significant shift in the first peak in $g_{OO}(r)$.

3.4. Validation of the Interionic Potentials. The cubic lattice parameter, *a*, given by the MD simulations at 300 K is in good agreement with those obtained experimentally (see Table 2). Furthermore, Figure 10 compares the final $G(r)$ values generated from the MD simulations (using eq 2) with those obtained from the neutron diffraction experiments, while Figure 11 plots the partial radial distribution functions for both $Zr_{0.8}Sc_{0.2}O_{1.9}$ and $Zr_{0.8}Y_{0.2}O_{1.9}$. The differences between the $g_{ZrO}(r)$ and $g_{YO}(r)$ in the latter material observed in the RMC analysis of the neutron diffraction data collected at room temperature are clearly reproduced. The good level of agreement between the experimental and simulated $G(r)$ and $g_{ij}(r)$ values indicates that the DIPPIM potentials provide an accurate description of the interactions between the ions in the $Zr_{0.8}Sc_{0.2-x}Y_xO_{1.9}$ system and can confidently be used to provide an insight into the local structural properties.

Turning to the ionic diffusion properties, the ionic conductivity can be estimated from the MD simulations using the Nernst–Einstein formula

$$\sigma_{NE} = c^2\rho D/k_BT \qquad (5)$$

where *c* is the charge of the mobile species, *ρ* is the system density, *D* is the diffusion coefficient, k_B is the Boltzmann constant, and *T* is the temperature. The diffusion coefficient, *D*, can be calculated from the slope of the mean square displacement of individual ions versus time at long times, that is,

$$D = \lim_{t\to\infty} \frac{1}{6N_{O^{2-}}} \langle \sum_{j=1}^{N_{O^{2-}}} [r_j(t) - r_j(0)]^2 \rangle \qquad (6)$$

Figure 12 shows that the calculated ionic conductivities successfully reproduce the observed trends in the experimental data with *x*, providing further validation of the reliability of the model for the interionic potentials adopted here.

3.5. Oxygen Vacancy Ordering. In principle, it is possible to extract information concerning any local ordering of the anion vacancies using the RMC analysis of the total neutron scattering data. While this process has been successfully applied to materials with relatively high vacancy concentrations (such as reduced ceria, $CeO_{2-\delta}$[51]), tests showed the relatively small number of vacancies present in the $Zr_{0.8}Sc_{0.2-x}Y_xO_{1.9}$ (5% of the anion sites) precludes such an approach here. Therefore, information concerning the short-range correlations between the vacancies has been extracted from the MD simulations performed at a temperature of 1200 K, which is chosen to mimic the conditions experienced by a solid electrolyte material in an operational SOFC.

The cations within the cubic fluorite crystal structure form a face centered cubic array. Within this sublattice there are tetrahedral (two per cation) and octahedral (one per cation) interstices and, in the case of an ideal stoichiometric fluorite compound, the former are fully filled with anions and the latter are completely empty. Thus, it is possible to assign each anion with an MD configuration to a particular cavity using the instantaneous positions of the cations within the simulation and, ignoring

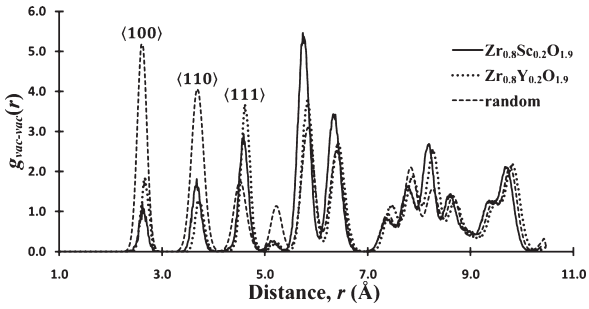

Figure 13. Vacancy−vacancy partial distribution function, $g_{vac-vac}(r)$, determined from the MD simulations at 1200 K for $Zr_{0.8}Sc_{0.2}O_{1.9}$ and $Zr_{0.8}Y_{0.2}O_{1.9}$.

Table 4. Relative Population of Vacancy Pairs in $Zr_{0.8}Sc_{0.2}O_{1.9}$ and $Zr_{0.8}Y_{0.2}O_{1.9}$ As Determined by MD Simulations

	$Zr_{0.8}Sc_{0.2}O_{1.9}$			$Zr_{0.8}Y_{0.2}O_{1.9}$		
T (K)	$n_{\langle 100\rangle}$	$n_{\langle 110\rangle}$	$n_{\langle 111\rangle}$	$n_{\langle 100\rangle}$	$n_{\langle 110\rangle}$	$n_{\langle 111\rangle}$
random	0.23	0.46	0.31	0.23	0.46	0.31
1000	0.01	0.21	0.77	0.06	0.10	0.84
1100	0.06	0.21	0.74	0.16	0.18	0.66
1200	0.13	0.25	0.62	0.17	0.19	0.65
1500	0.19	0.25	0.50	0.24	0.23	0.53
2000	0.28	0.33	0.39	0.24	0.30	0.46

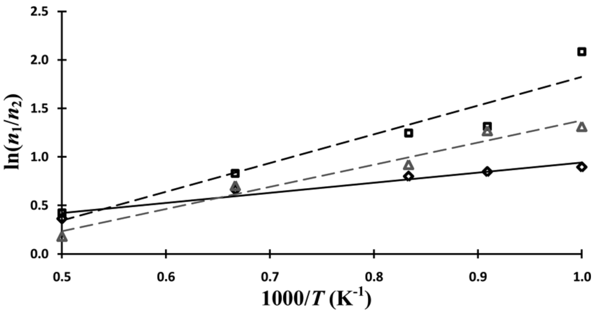

Figure 14. Logarithm of n_{Zr-vac}/n_{Y-vac} for $Zr_{0.8}Y_{0.2}O_{1.9}$ (solid black line) and the logarithm of $n_{\langle 111\rangle}/n_{\langle 110\rangle}$ for $Zr_{0.8}Y_{0.2}O_{1.9}$ (black dashed line) and $Zr_{0.8}Sc_{0.2}O_{1.9}$ (gray dashed line), versus reciprocal temperature.

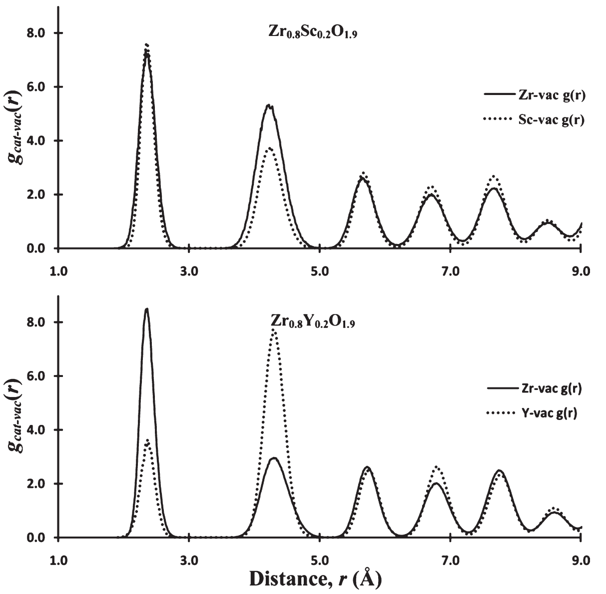

Figure 15. Cation−vacancy partial radial distribution functions determined by MD simulations at 1200 K for $Zr_{0.8}Sc_{0.2}O_{1.9}$ and $Zr_{0.8}Y_{0.2}O_{1.9}$.

the octahedral cavities (which are only very rarely occupied, even at the highest temperatures), define the locations of the anion vacancies as the centers of those tetrahedra which do not contain an anion. These locations can then be used to generate a vacancy−vacancy partial radial distribution function, $g_{vac-vac}(r)$ for each simulation. As shown in Figure 13, the two end members $Zr_{0.8}Sc_{0.2}O_{1.9}$ and $Zr_{0.8}Y_{0.2}O_{1.9}$ possess very similar $g_{vac-vac}(r)$ values, with a strong tendency to form pairs in ⟨111⟩ directions, rather than ⟨110⟩ or ⟨100⟩. This indicates that significant repulsive forces exist between individual anion vacancies and is consistent with diffraction studies of anion-deficient fluorite oxides[18,51] and so forth and the structural properties of ternary derivatives of zirconia.[30,32,33]

The temperature dependence of the relative population of the vacancy pairs in the ⟨100⟩, ⟨110⟩, and ⟨111⟩ directions is given in Table 4 for both $Zr_{0.8}Sc_{0.2}O_{1.9}$ and $Zr_{0.8}Y_{0.2}O_{1.9}$. Both materials show a strong variation with temperature, but there is no significant difference between the behavior of the Sc-doped and Y-doped materials, and the preference for vacancy pairs along ⟨111⟩ direction is maintained at the temperature range appropriate for SOFC applications, that is, 1000−1200 K. The data given in Table 4 can be used to calculate differences in the energies of different vacancy pairs, if it is assumed that the temperature dependence of their population follows an exponential behavior (as in a van't Hoff equation).[52] Taking the case of ⟨111⟩ and ⟨110⟩ vacancy pairs, it is possible to write

$$\frac{n_{\langle 110\rangle}}{n_{\langle 111\rangle}} = A_0 \times \exp\left(\frac{-E_{\langle 111\rangle - \langle 110\rangle}}{k_B T}\right) \qquad (7)$$

where A_0 is a constant, k_B Boltzmann's constant, and T the temperature in degrees kelvin. The energy difference, $E_{\langle 111\rangle-\langle 110\rangle}$, can be extracted from the data in Table 4 using a plot of the logarithm of $n_{\langle 111\rangle}/n_{\langle 110\rangle}$ against the inverse temperature. As shown in Figure 14, the linear fit confirms the validity of the above assumption and gives the energy difference $E_{\langle 111\rangle-\langle 110\rangle}$ as 0.20 and 0.23 eV for $Zr_{0.8}Sc_{0.2}O_{1.9}$ and $Zr_{0.8}Y_{0.2}O_{1.9}$, respectively, with the latter value in good agreement with that reported by Bogicevic et al.[53]

3.6. Cation−Vacancy Interactions. As illustrated in Figure 15, the cation−anion vacancy partial radial distribution functions are quite different between $Zr_{0.8}Sc_{0.2}O_{1.9}$ and $Zr_{0.8}Y_{0.2}O_{1.9}$. While both the Zr^{4+} and the Sc^{3+} cations in $Zr_{0.8}Sc_{0.2}O_{1.9}$ have an equal probability of being associated with a neighboring vacancy, $Zr_{0.8}Y_{0.2}O_{1.9}$ shows a significantly increased probability for its Zr^{4+} cations to attract an anion vacancy. The latter clearly indicates a strong interaction between the Zr^{4+} cations and the oxygen vacancies and suggests that this effect plays a major role in the decreased conductivity across the $Zr_{0.8}Sc_{0.2-x}Y_xO_{1.9}$ series.

Table 5 lists the percentage of vacancies located next to the host and dopant cations within $Zr_{0.8}Y_{0.2}O_{1.9}$, as extracted from the MD simulations performed over the temperature range from 1000 to 2000 K. These data can be used to estimate the difference in energy associated with an anion vacancy located next to a

Table 5. Percentage Number of Vacancies Next to Y and Zr, Respectively, in $Zr_{0.8}Y_{0.2}O_{1.9}$ As Determined by MD Simulations

T (K)	n_{Y-vac} (%)	n_{Zr-vac} (%)
1000	29	71
1100	30	70
1200	31	69
1500	34	66
2000	41	59

specific cation type, in a manner analogous to that used in the previous section for the case of vacancy−vacancy pairs. Thus,

$$\frac{n_{Zr - vac}}{n_{Y - vac}} = A_0 \times \exp\left(\frac{E_{Zr - Y}}{k_B T}\right) \qquad (8)$$

and a plot of the logarithm of n_{Zr-vac}/n_{Y-vac} against the inverse temperature gives a linear trend (see Figure 14) and an energy difference of E_{Zr-Y} = 0.09 eV. This value is also in good agreement with that reported by Bogicevic et al.[53] In the case of $Zr_{0.8}Sc_{0.2}O_{1.9}$, no significant preference for vacancies to be located close to either the Zr^{4+} or Sc^{3+} is observed, which corresponds to an E_{Zr-Sc} that is almost zero.

4. CONCLUSIONS

In this paper we assess the role of two processes, local ordering of the anion vacancies and their preference to reside close to a specific cation species, across the fluorite structured solid solution $Zr_{0.8}Sc_{0.2-x}Y_xO_{1.9}$ for $0.0 \le x \le 0.2$. The former appears largely independent of x, while there is a clear tendency for the vacancies to be located near to the host Zr^{4+} cations at the Y^{3+} rich end. Since the host and dopant cations are randomly distributed over all the cation sites, one might intuitively expect the two effects to be related. As an illustration, the alternative case of vacancies preferentially residing close to the (randomly distributed) Y^{3+} might then favor a more random distribution of vacancies, hinder the formation of vacancy pairs, and enhance the ionic conductivity. However, by associating with the more populous Zr^{4+} species there is little restriction on the spatial distribution of vacancies, and their tendency to form pairs in ⟨111⟩, driven by their strong repulsion at closer distances, dominates at all x. The decreasing ionic conductivity with increasing x is, therefore, dominated by cation−anion vacancy interactions and is associated with the presence of extensive strain within the lattice caused by the significant mismatch in size between the host Zr^{4+} and dopant Y^{3+} cations (as demonstrated by the partial radial distribution functions (see Figure 8)).

This paper demonstrates the ability of MD simulations, using interionic potentials developed with a strong ab initio basis and validated with respect to experimental data for the long-range structure, short-range ion−ion correlations, and ionic conductivity, to successfully probe the factors which influence the ionic diffusion processes. Indeed, it is particularly impressive in this case, given that the change in ionic conductivity across the $Zr_{0.8}Sc_{0.2-x}Y_xO_{1.9}$ series is only a factor of around two. In a subsequent paper[35] we will extend this methodology to probe the effects of vacancy−vacancy clustering and size mismatch between host and dopant cations in more detail and the presence of a maximum in the ionic conductivity of stabilized zirconias as a function of dopant concentration.

AUTHOR INFORMATION

Corresponding Author

*E-mail: stn@chalmers.se

Present Addresses

¶Department of Nuclear Science and Engineering, Massachusetts Institute of Technology.

ACKNOWLEDGMENT

The UK Science and Technology Facilities Council (STFC) is thanked for allocating beamtime at the ISIS Facility. S.T.N., I.A., and S.G.E. wish to thank Vetenskapsrådet (Swedish Research Council) for financial support. D.M. thanks the Moray Endowment Fund of the University of Edinburgh for the purchase of a workstation. D.M. also wishes to thank the UK Engineering and Physical Sciences Research Council (EPSRC), School of Chemistry, University of Edinburgh, and the STFC Centre for Materials, Physics and Chemistry (CMPC) for his Ph.D. funding. P.L. thanks the China Scholarship Council (CSC) for his Ph.D. funding.

REFERENCES

(1) Ormerod, R. M. *Chem. Soc. Rev.* **2003**, *32*, 17–28.
(2) Jiang, S. P.; Zhen, Y. D. *Solid State Ionics* **2008**, *179*, 1459–1464.
(3) Scott, H. G. *J. Mater. Sci.* **1975**, *10*, 1527–1535.
(4) Strickler, D. W.; Carlson, W. G. *J. Am. Ceram. Soc.* **1964**, *47*, 122–127.
(5) Morinaga, M.; Cohen, J. B.; Faber, J. *Acta Crystallogr., Sect. A* **1979**, *35*, 789–795.
(6) Morinaga, M.; Cohen, J. B.; Faber, J. *Acta Crystallogr., Sect. A* **1980**, *36*, 520–530.
(7) Welberry, T. R.; Withers, R. L.; Thompson, J. G.; Butler, B. D. *J. Solid State Chem.* **1992**, *100*, 71–89.
(8) Welberry, T. R.; Butler, B. D.; Thompson, J. G.; Withers, R. L. *J. Solid State Chem.* **1993**, *106*, 461–475.
(9) Welberry, T. R.; Withers, R. L.; Mayo, S. C. *J. Solid State Chem.* **1995**, *115*, 43–54.
(10) Ishizawa, N.; Matsushima, Y.; Hayashi, M.; Ueki, M. *Acta Crystallogr., Sect. B* **1999**, *55*, 726–735.
(11) Steele, D.; Fender, B. E. F. *J. Phys. C: Solid State Phys.* **1974**, *7*, 1–11.
(12) Faber, J.; Mueller, M. H.; Cooper, B. R. *Phys. Rev. B* **1978**, *17*, 4884–4888.
(13) Horiuchi, H.; Schultz, A. J.; Leung, P. C. W.; Williams, J. M. *Acta Crystallogr., Sect. B* **1984**, *40*, 367–372.
(14) Hull, S.; Farley, T. W. D.; Hackett, M. A.; Hayes, W.; Osborn, R.; Andersen, N. H.; Clausen, K.; Hutchings, M. T.; Stirling, W. G. *Solid State Ionics* **1988**, *28*−*30*, 488–492.
(15) Argyriou, D. N. *J. Appl. Crystallogr.* **1994**, *27*, 155–158.
(16) Kahlert, H.; Frey, F.; Boysen, H.; Lassak, K. *J. Appl. Crystallogr.* **1995**, *28*, 812–819.
(17) Argyriou, D. N.; Elcombe, M. M.; Larson, A. C. J. *Phys. Chem. Solids* **1996**, *57*, 183–193.
(18) Goff, J. P.; Hayes, W.; Hull, S.; Hutchings, M. T.; Clausen, K. N. *Phys. Rev. B* **1999**, *59*, 14202–14219.
(19) Hohnke, D. K. *Solid State Ionics* **1981**, *5*, 531–534.
(20) Catlow, C. R. A. *Solid State Ionics* **1984**, *12*, 67–73.
(21) Bogicevic, A.; Wolverton, C.; Crosbie, G. M.; Stechel, E. B. *Phys. Rev. B* **2001**, *64*, 014106.
(22) Mogensen, M.; Sammes, N. M.; Tompsett, G. A. *Solid State Ionics* **2000**, *129*, 63–94.
(23) Xia, C. R.; Liu, M. L. *Solid State Ionics* **2001**, *144*, 249–255.

(24) Ishihara, T.; Matsuda, H.; Takita, Y. *J. Am. Chem. Soc.* **1994**, *116*, 3801–3803.

(25) Huang, K. Q.; Tichy, R. S.; Goodenough, J. B. *J. Am. Ceram. Soc.* **1998**, *81*, 2565–2575.

(26) Huang, K. Q.; Tichy, R. S.; Goodenough, J. B. *J. Am. Ceram. Soc.* **1998**, *81*, 2576–2580.

(27) Huang, K. Q.; Tichy, R. S.; Goodenough, J. B. *J. Am. Ceram. Soc.* **1998**, *81*, 2581–2581.

(28) Sammes, M. N.; Tompsett, G. A.; Näfe, H.; Aldinger, F. *J. Eur. Ceram. Soc.* **1999**, *19*, 1801–1826.

(29) Fergus, J. W. *J. Power Sources* **2006**, *162*, 30–40.

(30) Fujimori, H.; Yashima, M.; Kakihana, M.; Yoshimura, M. *J. Am. Ceram. Soc.* **1998**, *81*, 2885–2893.

(31) Badwal, S. P. S.; Ciacchi, F. T.; Milosevic, D. *Solid State Ionics* **2009**, *136—137*, 91–99.

(32) Wurst, K.; Schweda, E.; Bevan, D. J. M.; Mohyla, J.; Wallwork, K. S.; Hofmann, M. *Solid State Sci.* **2003**, *5*, 1491–1497.

(33) Thornber, M. R.; Bevan, D. J. M.; Graham, J. *Acta Crystallogr., Sect. B* **1968**, *24*, 1183.

(34) Politova, T. I.; Irvine, J. T. S. *Solid State Ionics* **2004**, *168*, 153–165.

(35) Marrocchelli, D.; Madden, P. A.; Norberg, S. T.; Hull, S. *Chem. Mater.* **2011**, *23*, DOI: 10.1021/cm102809t.

(36) Hull, S.; Smith, R. I.; David, W. I. F.; Hannon, A. C.; Mayers, J.; Cywinski, R. *Physica B* **1992**, *180—181*, 1000–1002.

(37) Larson, A. C.; von Dreele, R. B. *General Structure Analysis System (GSAS)*; Los Alamos National Laboratory Report LAUR 86-748; Los Alamos National Laboratory: Los Alamos, NM, 1994.

(38) Soper A. K. (April 2010) Gudrun — A computer program developed for analysis of neutron diffraction data. http://www.isis.stfc.ac.uk/groups/disordered-materials/software/.

(39) Keen, D. A. *J. Appl. Crystallogr.* **2001**, *34*, 172–177.

(40) McGreevy, R. L. *J. Phys.: Condens. Matter* **2001**, *13*, R877–R913.

(41) Tucker, M. G.; Keen, D. A.; Dove, M. T.; Goodwin, A. L.; Hui, Q. *J. Phys.: Condens. Matter* **2007**, *19*, 335218.

(42) Norberg, S. T.; Tucker, M. G.; Hull, S. *J. Appl. Crystallogr.* **2009**, *42*, 179–184.

(43) Brese, N. E.; O'Keeffe, M. *Acta Crystallogr., Sect. B* **1991**, *47*, 192–197.

(44) Madden, P. A.; Heaton, R.; Aguado, A.; Jahn, S. *J. Mol. Struct.: THEOCHEM* **2006**, *771*, 9–18.

(45) Norberg, S. T.; Ahmed, I.; Hull, S.; Marrocchelli, D.; Madden, P. A. *J. Phys.: Condens. Matter* **2009**, *21*, 215401.

(46) Marrocchelli, D.; Madden, P. A.; Norberg, S. T.; Hull, S. *J. Phys.: Condens. Matter* **2009**, *21*, 405403.

(47) Marrocchelli, D.; Salanne, M.; Madden, P. A.; Simon, C.; Turq, P. *Mol. Phys.* **2009**, *107*, 443–452.

(48) Marrocchelli, D.; Salanne, M.; Madden, P. A. *J. Phys.: Condens. Matter* **2010**, *22*, 152102.

(49) Rietveld, H. M. *J. Appl. Crystallogr.* **1969**, *2*, 65–67.

(50) Shannon, R. D. *Acta Crystallogr., Sect. A* **1976**, *32*, 751–767.

(51) Hull, S.; Norberg, S. T.; Ahmed, I.; Eriksson, S. G.; Marrocchelli, D.; Madden, P. A. *J. Solid State Chem.* **2009**, *182*, 2815–2821.

(52) Atkins, P.; de Paula, J.; *Physical Chemistry*; Oxford University Press: New York, 2006.

(53) Bogicevic, A.; Wolverton, C. *Phys. Rev. B* **2003**, *67*, 024106.